

Nanoemulsions obtained via bubble bursting at a compound interface

Jie Feng¹, Matthieu Roché^{1, #}, Daniele Vigolo^{1, §}, Luben N. Arnaudov², Simeon D. Stoyanov^{2,3},

Theodor D. Gurkov⁴, Gichka G. Tsutsumanova⁵ and Howard A. Stone^{1, *}

1. Department of Mechanical and Aerospace Engineering, Princeton University, Princeton, New Jersey, 08544, USA

2. Unilever Research and Development, 3133AT Vlaardingen, The Netherlands

3. Laboratory of Physical Chemistry and Colloid Science, Wageningen University, 6703 HB Wageningen, The Netherlands;

Department of Mechanical Engineering, University College London, Torrington Place, London WC1E 7JE, UK

4. Department of Chemical Engineering, Faculty of Chemistry & Pharmacy, University of Sofia, Sofia 1164, Bulgaria

5. Department of Solid State Physics & Microelectronics, Faculty of Physics, University of Sofia, Sofia 1164, Bulgaria

[#] Present address: Laboratoire de Physique des Solides, Université Paris Sud-CNRS, 91405 Orsay, France

[§] Present address: Department of Chemistry and Applied Biosciences, Institute for Chemical and Bioengineering, ETH Zurich, 8093 Zurich, Switzerland

* Corresponding author: hastone@princeton.edu

18 **The bursting of bubbles at an air/liquid interface is a familiar occurrence**
19 **important to foam stability¹, cell cultures in bioreactors² and mass transfer between**
20 **the sea and atmosphere³⁻⁴. Here we document the hitherto unreported formation**
21 **and dispersal into the water column of submicrometre oil droplets following bubble**
22 **bursting at a compound air/oil/water-with-surfactant interface. We show that**
23 **dispersal results from the detachment of an oil spray from the bottom of the bubble**
24 **towards water during bubble collapse. We provide evidence that droplet size is**
25 **selected by physicochemical interactions between oil molecules and the surfactants**
26 **rather than by hydrodynamic effects. We illustrate the unrecognized role that this**
27 **dispersal mechanism may play in the fate of the sea surface micro-layer and of**
28 **pollutant spills by dispersing petroleum in the water column. Finally, our system**
29 **provides an energy-efficient route, with potential upscalability and wide**
30 **applicability, for applications in drug delivery⁵, food production⁶ and material**
31 **science⁷, which we demonstrate by producing polymeric nanoparticles.**

32 Previous studies of bubbles bursting at an air/water interface investigated mass
33 transfer from a lower liquid phase to a upper gas phase⁸⁻¹⁰, which also occurs when a
34 rising bubble passes through an oil/water interface¹¹. Here, we describe the reverse
35 transport process, where submicrometre oil droplets, formed during bubble bursting at a
36 compound interface are transported from the upper to the lower phase. We are not aware
37 of any previous documentation of this phenomenon. After continuous bubble bursting at
38 an air/hexadecane/water-with-surfactant interface for dozens of hours (Fig. 1a), the

39 aqueous phase became translucent, which suggested that small objects had been
40 dispersed in the lower water phase (Fig. 1b). The analysis of samples of the solution
41 using dynamic light scattering (DLS) confirmed the presence of objects with a radius $r \sim$
42 100 nm and a moderate polydispersity index (PDI, see Supplementary Materials) (Fig.
43 1c). Since the surfactant concentration in the water phase is well below the critical
44 micelle concentration¹² and we only observe submicrometre objects when there is
45 bubble bursting, these objects are oil droplets rather than spontaneously generated
46 microemulsion droplets or surfactant mesophases. Control experiments also confirm that
47 these submicrometre-sized droplets exist only when surfactants are present in the water
48 phase. Measurements of the size of hexadecane droplets on longer timescales showed
49 that r remained constant for at least a week (Fig. 1d). Thus, our experiments demonstrate
50 that the bursting of air bubbles at a compound interface also drives mass transport into
51 the bulk liquid to form stable submicrometre droplets.

52 High-speed visualization of the bubble bursting process from above the air/oil
53 interface and below the oil/water interface allowed us to understand how oil droplets are
54 dispersed in the surfactant solution. The bubble cap, initially formed of an oil film sitting
55 on a water film, bursts in two steps in most cases (Fig. 2a, Supplementary Movie 1). The
56 experimental images suggest that the top oil film retracts first and then the water film
57 breaks. Only the latter step induces droplet production through fragmentation of the
58 receding film, thus ruling out atomization of the bubble cap as the origin of the
59 submicrometre-sized oil droplets in the aqueous phase. A side view of the bursting

60 bubble below the oil/water interface reveals that oil droplets are dispersed from the
61 bottom of the bubble into the bulk water (Supplementary Movie 2). We have observed
62 that after a hole opens in the water film (blue circle in Fig. 2b.1) the surface of the cavity
63 deforms during film retraction (Fig. 2b.2) and a spray of droplets is ejected from the
64 cavity boundary towards the bulk water, at a location opposite to that of the nucleation
65 site of the hole (red circle in Figs. 2b.3-4). Also, we observed that the larger
66 non-Brownian droplets rose rapidly back to the oil/water interface, while the smaller
67 objects were ejected deep in the bulk water (Supplementary Movie 3). We speculate that
68 submicrometre-sized droplets are formed and dispersed during this spraying process,
69 although we cannot observe them directly with optical methods.

70 During the time that we observe droplet formation, the flow close to the
71 bubble-water interface resembles the boundary-layer detachment flow theoretically
72 predicted for the case of a bubble bursting at an air/water interface¹³: the separation of
73 the hydrodynamic boundary layer around the cavity means that streamlines detach
74 nearly perpendicular to the bubble boundary, which in our case leads to the spray into
75 the bulk fluid. We performed additional model experiments that show that 10- μm latex
76 particles initially sitting on the flat air/water interface without the oil phase are also
77 dispersed from the side of the cavity into the bulk water during bubble bursting in a
78 fashion similar to the oil droplets (Supplementary Movie 4). Thus, we propose the
79 dispersal mechanism summarized in Fig. 2c. For a bubble at the compound interface, the
80 upper oil film ruptures first, leaving a water film that retracts rapidly after a hole

81 nucleates on the bubble cap (Figs. 2c.1-3). Then, a spray of polydisperse droplets is
82 generated (Fig. 2c.4).

83 The similarity of the dispersal mechanism with the predicted boundary-layer
84 detachment motivated us to investigate how hydrodynamics may set the size of
85 submicrometre droplets. However, a study of this relationship with more than ten
86 non-aqueous phases and three surfactants in the aqueous phase (see Methods) shows that
87 the results are different from most fragmentation processes¹⁴⁻¹⁵. In particular, since the
88 size of the droplets r we measured is independent of a change of the initial thickness of
89 the oil layer h_I or the bubble diameter d_b (Figs. 3a,b), we used dimensional analysis to
90 determine a characteristic length scale for our system, which depends on viscosity of the
91 oil phase η_o , viscosity of the aqueous phase η_w , density of the oil phase ρ_o ($\approx \rho_w$) and the
92 interfacial tension between the oil and water γ_{ow} . Since $\eta_o \geq \eta_w$, we assume that only η_o is
93 significant, and we obtain $r \sim \eta_o^2 / (\rho_o \gamma_{ow})$. Unfortunately, this naive scaling law fails to
94 capture the three to five-fold decrease of r with a three-fold increase of η_o (Fig. 3c). In
95 addition, we observed that r increases with an increase of the speed of the last receding
96 film U_r (Fig. 3d), in contradiction with the expectation that an increase of the energy
97 injected in a two-phase liquid system generates smaller droplets¹⁵. Thus, the size of the
98 submicrometre droplets is independent of hydrodynamics.

99 We hypothesize that the submicrometre droplet size is set by molecular-scale
100 physicochemical interactions between the oil molecules and the surfactants. At the
101 macroscopic scale, these interactions translate into transitions between three possible

102 wetting states for oil on an aqueous surfactant solution depending on surfactant
103 concentration: partial, pseudo-partial and complete wetting¹⁶⁻¹⁸ (Fig. 4a). We found that
104 dispersal of submicrometre-sized droplets never occurred for liquid combinations
105 showing only a pseudo-partial-to-complete wetting transition (poly(dimethylsiloxane)
106 on aqueous surfactant solutions¹⁹) or partial wetting for all surfactant concentrations
107 (alkanes on aqueous solutions of Aerosol OT¹⁶). In contrast, dispersal occurred in
108 systems where only a surfactant-induced transition from partial to pseudo-partial wetting
109 happened. We observed the presence of oil droplets either when the equilibrium
110 surfactant concentration in water was high enough to induce a pseudo-partial wetting
111 state at rest, or when the surfactant concentration was smaller than the transition
112 concentration, but sufficiently close to it, so that surfactant compression²⁰ during bubble
113 bursting dynamics could trigger a wetting transition.

114 The correlation between the oil/water wetting state and the occurrence of dispersal
115 also suggests a possible explanation for the origin of the droplets. In our study, systems
116 showing pseudo-partial wetting involve linear alkanes and surfactants. Linear alkanes,
117 which are structurally similar to the hydrophobic moiety of the surfactants, can penetrate
118 the surfactant monolayer, and shorter alkanes penetrate more readily than longer alkanes.
119 As a consequence, the size of submicrometre alkane droplets obtained using a given type
120 of surfactant would increase as the length of the alkane carbon chain decreases^{9,21},
121 similar to what we observed (Fig. 3c). In addition, pseudo-partial wetting is
122 characterized by the coexistence of oil lenses at equilibrium with a thin film of oil whose

123 thickness is on the order of several molecular sizes¹⁷. These lenses could be the seeds of
124 our submicrometre droplets. To test this idea, we performed ellipsometry measurements
125 after the deposition of a millimeter-sized hexadecane droplet on a surfactant solution,
126 which show that small patches with a thickness on the order of 100 nm exist at places on
127 the interface (see Methods).

128 Next, we use this experimental result to deduce the lateral size and hence the volume
129 of the lenses so as to compare with the volume and the radius of the
130 submicrometre-sized droplets. The wetting state of oil/water+surfactant systems results
131 from a competition between short-range and long-range interactions described by the
132 initial spreading coefficient S_i and the Hamaker constant A , respectively¹⁷. Balancing
133 long-range van der Waals interactions with surface tension in a small slope
134 approximation gives

$$135 \quad A/h^3 \approx S_i h/\lambda^2, \quad (1)$$

136 where h is the lens thickness, which is on the order of 100 nm, and λ is the lateral size of
137 the lens (Fig. 4a; Supplementary Materials). Then, $\lambda \approx O(10 \mu\text{m})$, which is consistent
138 with other studies in pseudo-partial wetting²². The volume of one single lens is $V_{lens} \approx$
139 $h\lambda^2$ and then we expect the droplet volume $r^3 \approx h\lambda^2$. Hence $r \approx (h\lambda^2)^{1/3} \approx 10^{-6}$ m, which is
140 the order of magnitude of the size we measure. Direct confirmation of our hypotheses is
141 difficult experimentally due to the millisecond time scales and the submicrometre length
142 scales characteristic in our system, but the above arguments are consistent with all of our
143 observations.

144 The results we report here have important environmental consequences. For
145 example, we have verified that petroleum is dispersed in bulk water by bubble bursting
146 (Figs. 4b,c). For those environments where other well-identified mechanisms are limited,
147 the bubble-bursting process is one possibility to disperse oil into the lower water phase.
148 This dispersal may enhance pollution, where small droplets tend to be digested by sea
149 creatures more easily than on the surface, but dispersal may also help bacteria or algae to
150 degrade pollutants faster²³ because of the high surface-to-volume ratio of the droplets.
151 Also, the structural similarity between the compound interface that we study and the
152 interface separating the ocean from Earth's atmosphere, which is always covered by the
153 sea surface micro-layer (SML) containing surface-active organic matter²⁴, suggests that
154 the SML can be transported into the bulk of the oceans by bursting bubbles²⁵. For the
155 above scenarios, we are not aware of any study investigating mass transfer from the
156 surface of the ocean towards its bulk due to bubble bursting, which has been related so
157 far only to the formation of wind-dispersed aerosols²⁶.

158 Inspired by the application of bubbling to the production of colloids²⁷ and
159 liposomes²⁸, our study provides a potential scalable route for the production of
160 dispersions of submicrometre particles. As an illustration, we have dispersed droplets of
161 a polymer liquid (NOA 89) and we cross-linked it using UV light to obtain solid
162 particles with a size comparable to that of the original droplets (Figs. 4d,e; Methods).
163 Our dispersal method meets three requirements important to industry. First, its energy
164 efficiency is 1 - 10%, which is at least one order of magnitude greater than the $O(0.1\%)$

165 efficiency of classical high-shear-rate methods²⁹ (see Supplementary Materials for
166 detailed calculations). Second, bubble bursting has potential to be scaled up, by
167 increasing bubbling frequency for example (see Supplementary Materials), while
168 keeping costs low and remaining sustainable, in contrast with the mechanical top-down
169 methods. Finally, compared to classical self-emulsification for nanoemulsions³⁰, which
170 only works for specific compounds having ultra-low interfacial tensions, our system
171 works even when interfacial tensions are on the order of tens of mN/m and thus it has
172 broad applicability.

173

174

175

176

177

178

179

180

181

182

183

184

185

186 **Methods**

187 **Experimental system** The experimental system is shown in Fig. 1a. For each
188 experiment, a thin layer of the dispersed phase, e.g. a non-polar oil, was deposited on an
189 aqueous solution containing an ionic surfactant C_n TAB. Air bubbles were formed at the
190 tip of a tube located at the bottom of the tank. The bubbles rose to the interface because
191 of buoyancy. We changed the size of the bubbles by adjusting the injection pressure and
192 the diameter of the tube. The bubbling frequency was adjusted to 0.1-1 Hz and we made
193 sure there were at most a few bubbles at the interface without forming a bubble column.
194 Each experiment ran for 48 hours to produce enough submicrometre droplets to be
195 detected. To reduce the influence of dust, the container was made clean before each
196 experiment. During the experiment, we reduced the contamination of the interface and
197 the bulk by covering the tank. We collected samples deep in the bath and far from the
198 interface. Samples were analyzed with DLS 8 hours after sampling without any further
199 treatment. The high-speed camera was applied to capture the bubble-bursting process
200 while ellipsometry was utilized for observation of the oil layer at the interface. The
201 UV-cured experiments were carried out using a UV oven (IntelliRay 400, Uvitron) to
202 crosslink the particles. The UV wavelengths were within the range 320–390 nm and the
203 exposure time was 15 s.

204 **Materials** An aqueous surfactant solution was used as the continuous phase.
205 Ultrapure water (resistivity 18.2 M Ω , Millipore MilliQ) was used to prepare all solutions.
206 We used the surfactants C_{16} TAB (Hexadecyltrimethylammonium bromide,

207 Sigma-Aldrich, BioXtra, $\geq 99\%$), C_{12} TAB (Dodecyltrimethylammonium bromide,
208 Sigma-Aldrich, BioXtra, $\sim 99\%$) and Aerosol OT (Docusate sodium, Sigma-Aldrich)
209 were applied in the experiments as the water-soluble surfactants. For the oil phase, we
210 used n-hexadecane (Sigma-Aldrich, anhydrous, $\geq 99\%$, $\rho = 773 \text{ kg/m}^3$, $\eta = 3.03 \text{ mPa}\cdot\text{s}$ at
211 25°C), n-pentadecane (Sigma-Aldrich, $\geq 99\%$, $\rho = 769 \text{ kg/m}^3$, $\eta = 2.56 \text{ mPa}\cdot\text{s}$ at 25°C),
212 n-tetradecane (Sigma-Aldrich, olefine free, $\geq 99\%$, $\rho = 762 \text{ kg/m}^3$, $\eta = 2.10 \text{ mPa}\cdot\text{s}$ at 25°C),
213 n-tridecane (Sigma-Aldrich, $\geq 99\%$, $\rho = 756 \text{ kg/m}^3$, $\eta = 1.71 \text{ mPa}\cdot\text{s}$ at 25°C), n-dodecane
214 (Sigma-Aldrich, anhydrous, $\geq 99\%$, $\rho = 750 \text{ kg/m}^3$, $\eta = 1.38 \text{ mPa}\cdot\text{s}$ at 25°C), n-undecane
215 (Sigma-Aldrich, $\geq 99\%$, $\rho = 740 \text{ kg/m}^3$, $\eta = 1.15 \text{ mPa}\cdot\text{s}$ at 25°C), n-decane (Sigma-Aldrich,
216 anhydrous, $\geq 99\%$, $\rho = 730 \text{ kg/m}^3$, $\eta = 0.92 \text{ mPa}\cdot\text{s}$ at 25°C), and poly(dimethylsiloxane)
217 (Sigma-Aldrich, $\nu = 1, 5$ or 10 cSt at 25°C). The UV-cured material in Figs. 4d and e is
218 Norland Optical Adhesive 89 which is cured by ultraviolet light with maximum
219 absorption within the range of 310-395 nm.

220 **High-speed imaging** A high-speed camera (Vision Research, Phantom V7.3) with a
221 lens (Sigma, DG Macro 105 mm) was used to record high-speed videos of the bubble
222 collapse, at frame rates from 6800 up to 32000 fps. Movies were processed using Fiji
223 software.

224 **Dynamic light scattering** The size of the submicrometre droplets was determined
225 by dynamic light scattering (DLS) using a Malvern Zetasizer Nano ZS. The
226 measurements were performed at 12.8° or 173° scattering angle with 4 mW He-Ne laser
227 producing light with wavelength of 633 nm. DLS data were processed with Malvern's

228 software using a distribution analysis based on a cumulant model to fit a single
229 exponential to the correlation function to obtain the cumulant mean size and size
230 distribution of the submicrometre droplets. The cumulant analysis is defined in ISO
231 standard document 13321. The calculations of PDI are defined in the ISO standard
232 document 13321:1996 E. Results of the PDI in different measurements were shown in
233 Supplementary Materials.

234 **Ellipsometry** Ellipsometry experiments are carried out in the following way:
235 polarized laser light (with wavelength 532 nm) was shined at the surface of a Petri dish
236 with an aqueous solution of $[C_{16}TAB] = 0.9$ mM and the reflected signal was recorded
237 with a detector. The setup is based on a null type ellipsometer (LEF 3M, Novosibirsk,
238 Russia), equipped with a rotating analyzer unit that allows to measure the changes in
239 reflected light polarization in time steps of ~ 0.2 seconds. The angle of incidence is 50.0° .
240 The instrument records the ellipsometric angles Ψ , Δ , where $\tan\Psi\exp(i\Delta)$ is the
241 polarization ratio of the output to the input signal. The technique is described in detail
242 elsewhere³¹. As the laser spot has a finite dimension (~ 1 mm²), the values of Ψ , Δ are the
243 average ones for the entities present in this spot. When stable base lines at the air/
244 aqueous C₁₆TAB boundary were established, a drop of 10 μ L hexadecane was carefully
245 added on the interface (far from the laser beam), and changes in polarization were
246 detected, which in turn allow the calculation of the film thickness (assuming a refractive
247 index of hexadecane $n = 1.4340$).

248

249 **References**

- 250 1. Tong, M., Cole, K. & Neethling, S. J. Drainage and stability of 2D foams: foam
251 behaviour in vertical Hele-Shaw cells. *Colloid Surface A* **382**, 42-49 (2011).
- 252 2. Moheimani, N. R., Isdepsky, A., Lisec, J., Raes, E. & Borowitzka, M. A.
253 Coccolithophorid algae culture in closed photobioreactors. *Biotechnol. Bioeng.* **108**,
254 2078-2087 (2011).
- 255 3. Wu, J. Evidence of sea spray produced by bursting bubbles. *Science* **212**, 324-326
256 (1981).
- 257 4. Schmitt-Kopplin, P. *et al.* Dissolved organic matter in sea spray: a transfer study
258 from marine surface water to aerosols. *Biogeosciences* **9**, 1571-1582 (2012).
- 259 5. Wang, L. J., Dong, J. F., Chen, J., Eastoe, J. & Li, X. F. Design and optimization of a
260 new self-nanoemulsifying drug delivery system. *J. Colloid Interf. Sci.* **330**, 443-448
261 (2009).
- 262 6. Rao, J. & McClements, D. J. Food-grade microemulsions and nanoemulsions: role of
263 oil phase composition on formation and stability. *Food Hydrocolloid* **29**, 326-334
264 (2012).
- 265 7. Mason, T. G., Wilking, J. N., Meleson, K., Chang, C. B. & Graves, S. M.
266 Nanoemulsions: formation, structure, and physical properties. *J. Phys-Condens Mat.*
267 **18**, R635-R666 (2006).
- 268 8. Duchemin, L., Popinet, S., Josserand, C. & Zaleski, S. Jet formation in bubbles
269 bursting at a free surface. *Phys. Fluids* **14**, 3000-3008 (2002).

- 270 9. Bird, J. C., de Ruiter, R., Courbin, L. & Stone, H. A. Daughter bubble cascades
271 produced by folding of ruptured thin films. *Nature* **465**, 759-762 (2010).
- 272 10. Lhuissier, H. & Villermaux, E. Bursting bubble aerosols. *J. Fluid Mech.* **696**, 5-44
273 (2012).
- 274 11. Uemura, T., Ueda, Y. & Iguchi, M. Ripples on a rising bubble through an immiscible
275 two-liquid interface generate numerous micro droplets. *Europhys. Lett.* **92**, 34004
276 (2010).
- 277 12. Mukerjee, P. & Mysels, K. J. Critical micelle concentrations of aqueous surfactant
278 systems. (U.S. National Bureau of Standards; for sale by the Supt. of Docs., U.S.
279 Govt. Print. Off., 1971).
- 280 13. Boulton-Stone, J. M. & Blake, J. R. Gas-bubbles bursting at a free surface. *J. Fluid*
281 *Mech.* **254**, 437-466 (1993).
- 282 14. Eggers, J. & Villermaux, E. Physics of liquid jets. *Rep. Prog. Phys.* **71**, 036601
283 (2008).
- 284 15. Walstra, P. Principles of emulsion formation. *Chem. Eng. Sci.* **48**, 333-349 (1993).
- 285 16. Wilkinson, K. M., Bain, C. D., Matsubara, H. & Aratono, M. Wetting of surfactant
286 solutions by alkanes. *ChemPhysChem* **6**, 547-555 (2005).
- 287 17. Ash, P. A., Bain, C. D. & Matsubara, H. Wetting in oil/water/surfactant systems.
288 *Curr. Opin. Colloid. In.* **17**, 196-204 (2012).
- 289 18. Kellay, H., Meunier, J. & Binks, B. P. Wetting properties of normal-alkanes on AOT
290 monolayers at the brine-air interface. *Phys. Rev. Lett.* **69**, 1220-1223 (1992).

- 291 19. Cheng, Y., Ye, X., Huang, X. D. & Ma, H. R. Reentrant wetting transition on
292 surfactant solution surfaces. *J. Chem. Phys.* **125**, 164709 (2006).
- 293 20. Boulton-Stone, J. M. The effect of surfactant on bursting gas-bubbles. *J. Fluid Mech.*
294 **302**, 231-257 (1995).
- 295 21. Evans, D. F. & Wennerström, H. k. *The Colloidal Domain : where physics, chemistry,*
296 *biology, and technology meet.* 2nd edn (Wiley-VCH, 1999).
- 297 22. Takata, Y. et al. Line tension and wetting behavior of an air/hexadecane/aqueous
298 surfactant system. *Langmuir* **21**, 8594-8596 (2005).
- 299 23. Cormack, D. *Response to Marine Oil Pollution - Review and Assessment* (Springer,
300 1999).
- 301 24. Wurl, O., Wurl, E., Miller, L., Johnson, K. & Vagle, S. Formation and global
302 distribution of sea-surface microlayers. *Biogeosciences* **8**, 121-135 (2011).
- 303 25. Sellegri, K., O'Dowd, C. D., Yoon, Y. J., Jennings, S. G. & de Leeuw, G. Surfactants
304 and submicron sea spray generation. *J. Geophys. Res-Atmos.* **111**, D22215 (2006).
- 305 26. Brock, C. A., Murphy, D. M., Bahreini, R. & Middlebrook, A. M. Formation and
306 growth of organic aerosols downwind of the Deepwater Horizon oil spill. *Geophys.*
307 *Res. Lett.* **38**, L17805 (2011).
- 308 27. Arnaudov, L. N., Stoyanov, S. D. & Stuart, M. A. C. Colloid fabrication by
309 co-extrusion. *Colloid Surface A* **323**, 94-98 (2008).
- 310 28. Talsma, H., Vansteenbergen, M. J., Borchert, J. C. H. & Crommelin, D. J. A. A novel
311 technique for the one-step preparation of liposomes and nonionic surfactant vesicles

312 without the use of organic solvents. Liposome formation in a continuous gas-stream:
313 the bubble method. *J. Pharm. Sci.* **83**, 276-280 (1994).

314 29. Solans, C. & Sole, I. Nano-emulsions: formation by low-energy methods. *Curr.*
315 *Opin. Colloid In.* **17**, 246-254 (2012).

316 30. Rosen, M. J. & Kunjappu, J. T. *Surfactants and Interfacial Phenomena*. 4th edn
317 (Wiley, 2012).

318 31. Russev, S. C. & Arguirov, T. V., Rotating analyzer-fixed analyzer ellipsometer based
319 on null type ellipsometer, *Rev. Sci. Instrum.*, **70**, 3077-3082 (1999).

320

321 **Acknowledgments**

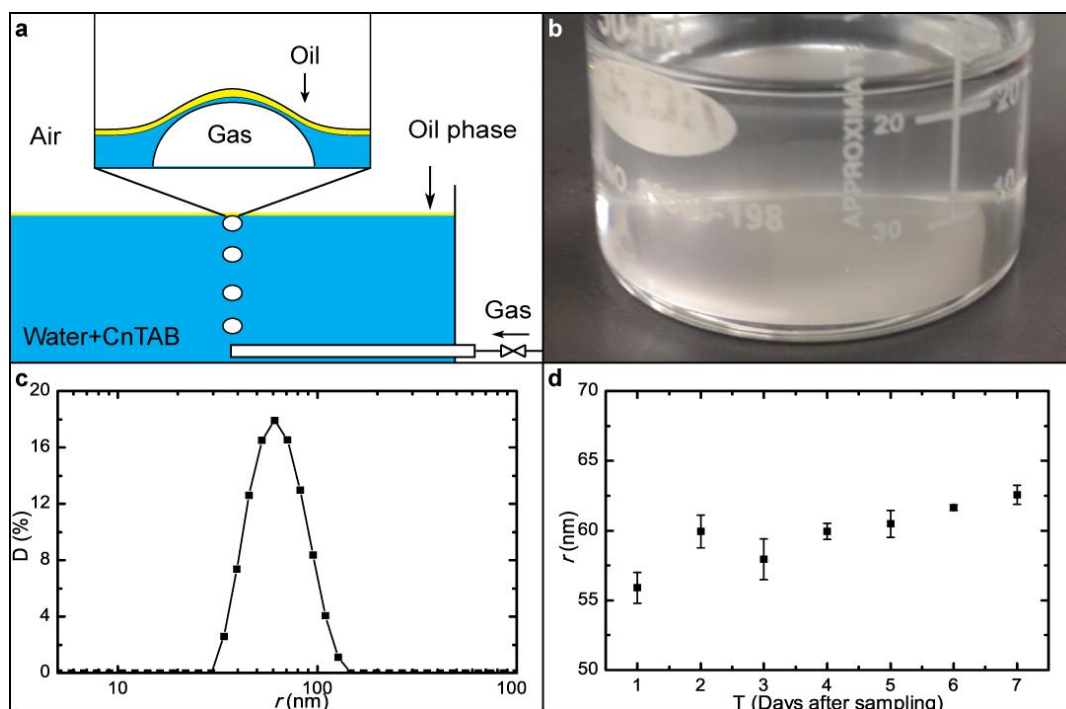
322 We acknowledge the contribution of S. C. Russev from Department of Solid State
323 Physics & Microelectronics, University of Sofia, Bulgaria who helped us with the
324 interpretation of the ellipsometric data and R. D. Stanimirova from Department of
325 Chemical Engineering, University of Sofia, Bulgaria, who performed measurements in a
326 Langmuir trough and some spreading experiments. T. D. G. and S. D. S. acknowledge
327 the financial support of EU project FP7-REGPOT-2011-1, “Beyond Everest”. M. R.
328 acknowledges D. Langevin for fruitful discussions. H. A. S. thanks the NSF for support
329 via grant CBET.

330

331

332

333 **Figure Legends**



334

335 **Figure 1 | Bubble bursting at an air/oil/water interface.** (a) Sketch of the experimental system.
 336 Inset: close-up of the deformed compound interface. (b) Image of the translucent aqueous phase
 337 after bubbling for 48 hours (Oil phase: dodecane, aqueous phase: $[C_{16}TAB] = 0.09$ mM). (c) Size
 338 distribution of the oil droplets based on the intensity measured by DLS (Oil phase: hexadecane,
 339 initial thickness of the oil layer $h_l = 1$ mm; bubble diameter $d_b = 2.8 \pm 0.25$ mm, aqueous phase:
 340 $[C_{16}TAB] = 0.09$ mM). The peak value of the distribution (59.8 nm here, with PDI = 0.091) is
 341 taken as the radius of the submicrometre droplets. (d) Time evolution of the size of the
 342 submicrometre droplets in the same sample shown in Fig. 1c over a week, which demonstrates
 343 stability of the submicrometre droplets. The error bar here is defined as the standard deviation of
 344 the droplet size in three DLS measurements.

345

346

347

348

349

350

351

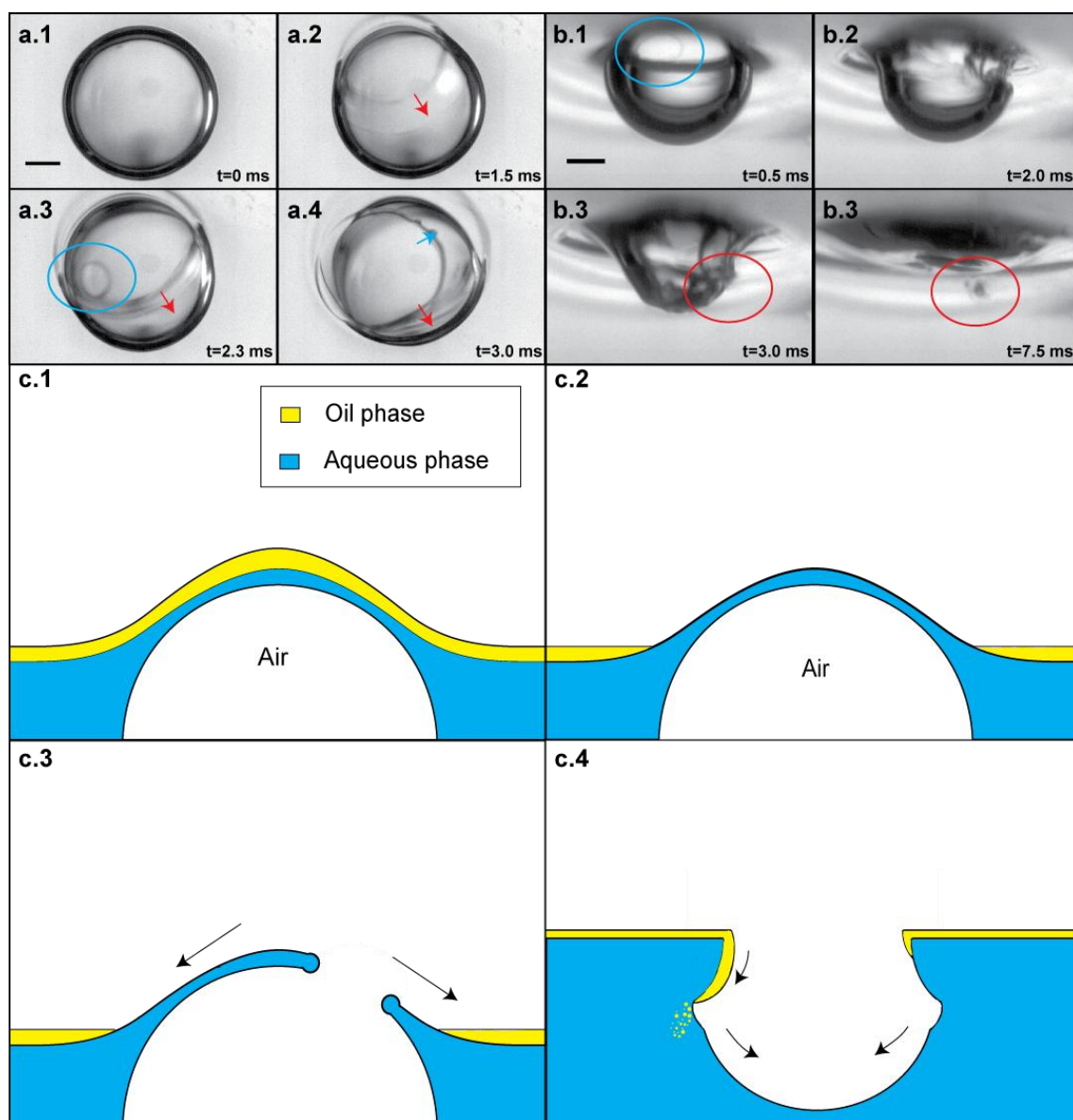
352

353

354

355

356



358

359 **Figure 2 | High-speed observations of the bursting process and schematic descriptions for**
 360 **the dispersal mechanism.** (a) Top-view photos of the bursting of a bubble at interfaces of
 361 air/hexadecane/water at $[C_{16}TAB] = 0.09$ mM ($h_l = 1$ mm; $d_b = 4.0 \pm 0.21$ mm; scale bar is 1
 362 mm): a.1, The bubble rests near the compound interface with oil and water films on top of the
 363 bubble; a.2, The oil film (above the water film) ruptures first before the water film. The
 364 retraction direction of the oil film is shown with the red arrow; a.3, After the rupture of the oil
 365 film, a hole opens in the water film, as shown with the blue circle; a.4, The water film then
 366 retracts along a direction different from that of the oil film. The retraction direction of the
 367 water film is shown with the blue arrow. b. Side-view photos of the bursting of a bubble at interfaces
 368 of air/hexadecane/water at $[C_{16}TAB] = 0.09$ mM ($h_l = 1$ mm; $d_b = 4.0 \pm 0.21$ mm; scale bar is 1
 369 mm). b.1, A hole is nucleated on the cap of the bubble, as shown with the blue circle; b.2, The
 370 surface of the cavity deforms; b.3, The deformation propagates further down the interface; b.4, A

371 spray of droplets is created at the wall of the cavity, as shown with the red circle. Note that (a)
372 and (b) are not taken simultaneously. c. Sketch of mechanism for the dispersal formation.

373

374

375

376

377

378

379

380

381

382

383

384

385

386

387

388

389

390

391

392

393

394

395

396

397

398

399

400

401

402

403

404

405

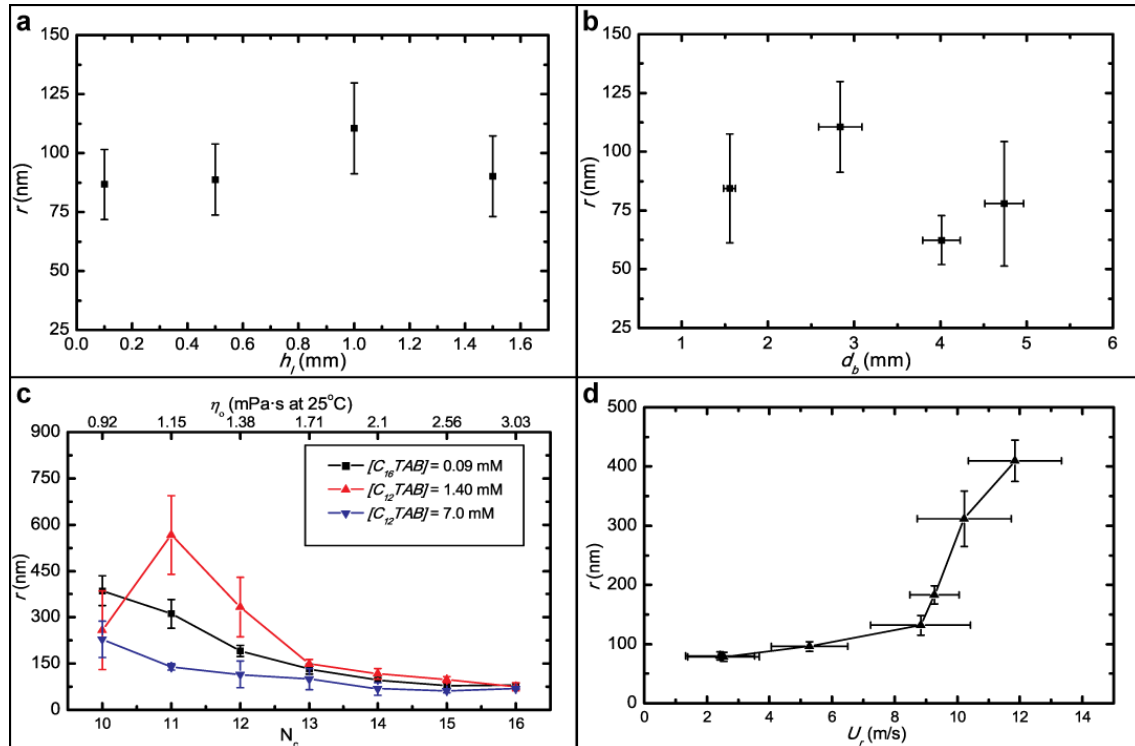
406

407

408

409

410



411

412

413

414

415

416

417

418

419

420

421

422

423

424

425

426

427

428

429

430

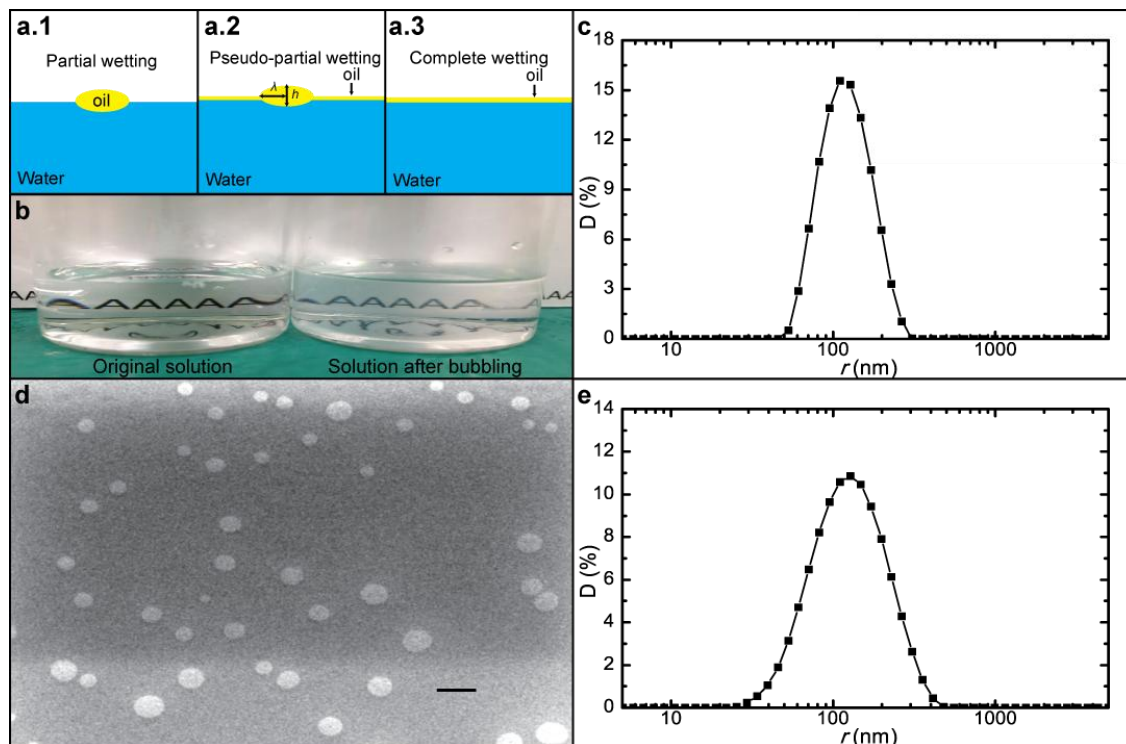
431

432

433

434

Figure 3 | Influence of oil thickness (h_l), bubble diameter (d_b), viscosity of oil (η_o) and carbon number (N_c) of the oil on the size of the submicrometre-sized droplets (r). (a) Relationship between r and h_l (Oil phase: hexadecane; $d_b = 2.8 \pm 0.25$ mm; aqueous phase: $[C_{16}TAB] = 0.09$ mM). (b) Relationship between r and d_b (Oil phase: hexadecane; $h_l = 1$ mm; aqueous phase: $[C_{16}TAB] = 0.09$ mM). (c) Relationship between r and η_o as well as N_c (Oil phase: hexadecane; $h_l = 1$ mm; $d_b = 2.8 \pm 0.25$ mm; aqueous phase: $[C_{16}TAB] = 0.09$ mM and $[C_{12}TAB] = 1.40$ mM or 7.0 mM. Note that r for $N_c = 11$ with $[C_{12}TAB] = 1.40$ mM was determined by microscope using image analysis since DLS could not obtain a reliable correlation function for these samples. (d) Relationship between r and the speed of the last receding film U_r .



436

437

Figure 4 | Sketch of different wetting states and formation of petroleum dispersal and

438

polymeric submicrometre particles. (a) Partial wetting, pseudo-partial wetting and complete

439

wetting behaviors of an oil drop on an aqueous surface. The partial wetting state is characterized

440

by an oil lens sitting at the air/water interface in equilibrium with a two-dimensional dilute gas

441

of oil molecules while, in the pseudo-partial wetting state, the oil initially spreads after

442

deposition and then forms lenses in equilibrium with a microscopic film of a few molecules

443

thick. The oil spreads out to form a film of uniform thickness covering the whole surface in the

444

complete wetting state. (b) Image of the aqueous phase after bubbling for 48 hours using

445

petroleum as the oil phase ($h_l = 1$ mm; $d_b = 2.8 \pm 0.25$ mm; aqueous phase: $[C_{16}TAB] = 0.09$

446

mM). The solution after bubbling is hazy compared with the original solution. (c) Results of

447

DLS measurement for samples of the solution after bubbling. The size of the droplets is 113.4

448

nm with PDI = 0.101. (d) ESEM photo of UV-cured submicrometre particles produced by

449

bubble bursting (Oil phase: Norland Optical Adhesive (NOA) 89; $h_l = 1$ mm; $d_b = 2.8 \pm 0.25$ mm;

450

aqueous phase: $[C_{16}TAB] = 0.09$ mM). Scale bar is 500 nm. (e) DLS results of the NOA 89

451

sample before the UV-cured process. The size of the particles is 109.8 nm with PDI = 0.197.